Effect of Cooling Rate on Magnetic Properties of FeCoNi(CuAl)$_{0.8}$ High Entropy Alloy

Xiangyun Zhang*, Ding Guoqiang, Dong Jiao, and ZiZhou Yuan

State Key Laboratory of Advanced Processing and Recycling of Nonferrous Metals, Lanzhou University of Technology, Lanzhou 730050, China

The solidification process of an alloy has a significant influence on its microstructure and properties. In this article, the effect of cooling rate on the microstructure and magnetic properties of the FeCoNi(CuAl)$_{0.8}$ high entropy alloys (HEAs) was investigated. Results showed that all the samples prepared at different cooling rates exhibited a duplex-phase structure of face-centered cubic (FCC) plus body-centered cubic (BCC). But the volume fraction of BCC and stacking density of the alloy increased with the increasing of cooling rate, leading to an increase in saturated magnetization. Furthermore, microstructure investigation showed that with the increasing of cooling rate, the grain size of the samples decreased, lattice distortion and residual stress increased, and more nanoprecipitates were embedded in the interdendritic phases of the sample, which may be responsible for the increase in coercivity of the alloy.

Keywords : high entropy alloys, cooling rate, magnetic properties

1. Introduction

Because of the high entropy effect, severe lattice distortion effect and cocktail effect, high-entropy alloys have many excellent properties [1-3]. For example, FeCoNi(CuAl)$_{0.8}$ high entropy alloys (HEAs) with duplex-phase of body-centered cubic (BCC) and face-centered cubic (FCC) phases not only exhibit high compressive strength (2219 MPa) and good plasticity (47.8 %) [4], but also have good soft magnetic properties due to the large amount of ferromagnetic elements such as Fe, Co and Ni [5]. Therefore, HEAs have great potential in practical application, such as jet-engine turbines, electric motors and electronic communications [6-8].

As is known to all, the properties of an alloy depend largely on the solidification process. Cooling rate can promote the formation of different microstructures, and obtain different mechanical properties. For example, compared to the ordinary crystalline alloy, the amorphous alloy prepared by high cooling rate always exhibits ultrahigh strength and better soft magnetic properties [9, 10]. Wei *et al.* [11, 12] found that HEAs metallic glass with

nanoscale FCC phase embedded in glass matrix with excellent saturated magnetization (M_s) and low coercivity (H_c) can be obtained by rapid cooling. Therefore, it may be possible to refine the grains and improve the magnetic properties by increasing the cooling rate of the alloy. The effects of cooling rate on mechanical properties such as strength, plasticity [13] and hardness [14] of various HEAs have been widely studied. However, up to now, the effect of cooling rate on the microstructure and magnetic properties of HEAs with duplex-phase is still unclear.

In general, parameters for soft magnetic alloys such as M_s, maximum magnetic flux density (B_m), and remanence (B_r) are mainly determined by crystal structure and composition, while H_c, permeability (m_i) and maximum permeability (m_{max}) are primarily affected by internal stress, grain size, impurity, and heat treatment etc [5]. Besides grain size, crystal structure and composition segregation of HEAs may be changed during the solidification process with different cooling rates. According to [15], in quenching molten alloys, the typical dimension of a sample is inversely proportional to the square of the sample diameter. Therefore, in this paper, the effect of cooling rates on microstructure and magnetic properties of FeCoNi(CuAl)$_{0.8}$ HEAs is explored in detail through preparation of samples with different diameters.

*Corresponding author: Tel: +86-13109322559
e-mail: zhangxiangyun86@163.com

2. Experimental Procedure

To ensure chemical homogeneity, alloy ingots with a nominal composition of FeCoNi(CuAl)$_{0.8}$ were prepared by arc melting of high-purity metals (>99.9 wt%) in a water-cooled copper crucible under high-purity argon atmosphere at least seven times. The master ingots were then sucked into a water-cooled copper mold to obtain cylindrical rods with various diameters of 2 mm, 4 mm, and 6 mm, and a length of 50 mm. The master ingot with an oblate spheroid shape of approximately 16 mm in diameter and 6 mm in thickness was denoted as the AM alloys.

The structures of the alloys were characterized by D8ADVANCE X-ray diffraction (XRD) with Cu Kα radiation. The microstructures of the alloys were characterized by a JSM 6700F scanning electron microscope (SEM) with an energy dispersive spectrometer (EDS). The further detailed phase structure and element distribution were investigated by a JEOL 2100F transmission electron microscope (TEM) with an energy dispersive X-ray spectroscopy (EDX). The lamellar TEM specimens were prepared by room temperature Gatan PIPS ion milling with a working distance of ±10° tilt angle. The magnetic properties of all the samples were examined by a Squid MPMS3 vibrating sample magnetometer (VSM) during an internal magnetic field of 2.0 T. Magnetic detection samples with diameter of 2 mm and thickness of a 300 microns were cut from the center of the samples by an IsoMet 1000 precision cutting machine at room temperature.

3. Results and Discussion

3.1. Magnetic properties

Fig. 1 shows the hysteresis loops of FeCoNi(CuAl)$_{0.8}$ HEAs with different cooling rate. All the samples are typical soft magnetic alloys with M_s from 77.7 to 81.6 A·m^2/Kg and low H_c of 480-777 A/m. M_s and H_c of the samples with different cooling rates are presented in table 1 and Fig. 1(b). It can be seen that the AM sample and 6 mm sample nearly have the same M_s and H_c, and then the values of M_s and H_c gradually increase with the increasing of cooling rate.

3.2. Microstructure analysis

Fig. 2 shows XRD patterns of the alloys with different cooling rates. It can be seen that all the samples exhibit duplex-phase structure of face-centered cubic (FCC) plus body-centered cubic (BCC). The ratio of the strongest peak of FCC and BCC phase for the same XRD curve,
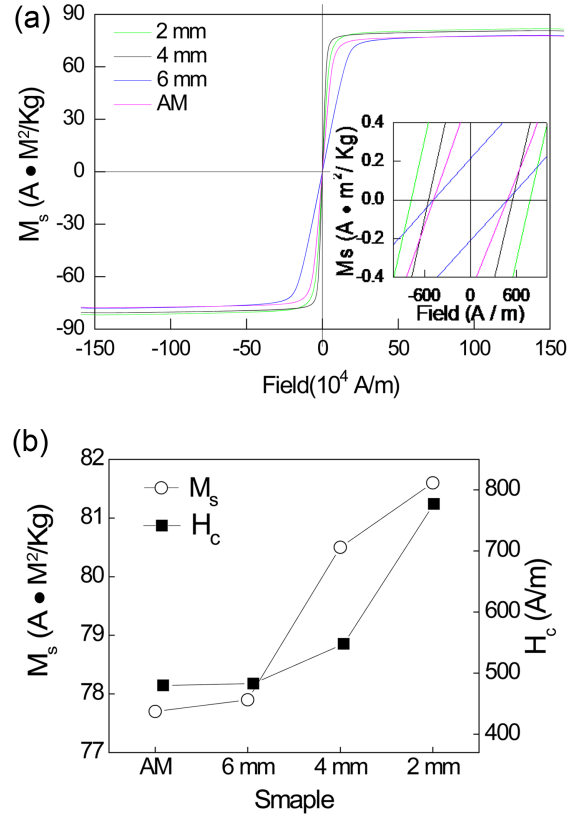

Fig. 1. (Color online) Hysteresis loops (a) and magnetic parameters (b) of FeCoNi(CuAl)$_{0.8}$ HEAs at various cooling rates.

Table 1. Intensity ratio and lattice constants of the FCC and BCC phases for the alloys.

Alloys	Lattice parameters (Å)		$I_{(111)F}/I_{(110)B}$	M_s (A·m^2/Kg)	H_c (A/m)
	FCC	BCC			
AM	3.618	2.8634	1.96	77.7	480
6 mm	3.615	2.8625	1.872	77.9	483
4 mm	3.6143	2.8622	1.79	80.5	548
2 mm	3.6114	2.8622	1.675	81.6	777

namely $I_{(111)F}/I_{(110)B}$, is used to describe the content of FCC phase and BCC phase. Based on the XRD data, the calculated $I_{(111)F}/I_{(110)B}$ and lattice constants are listed in Table 1. The volume fraction of the BCC phase measured was ~33.78 %, ~34.82 %, ~35.84 %, and ~37.38 % for the AM sample, 6 mm sample, 4 mm sample, and 2 mm sample, respectively, indicating that the relative volume fraction of BCC increases with the increasing of cooling rate. According to Wei [11], BCC Fe is ferromagnetic, but the ferromagnetism is counteracted when the Fe atoms are arranged in a closely packed configuration, such as an FCC lattice. HEAs with a BCC structure usually exhibit higher saturation magnetization than those with an FCC
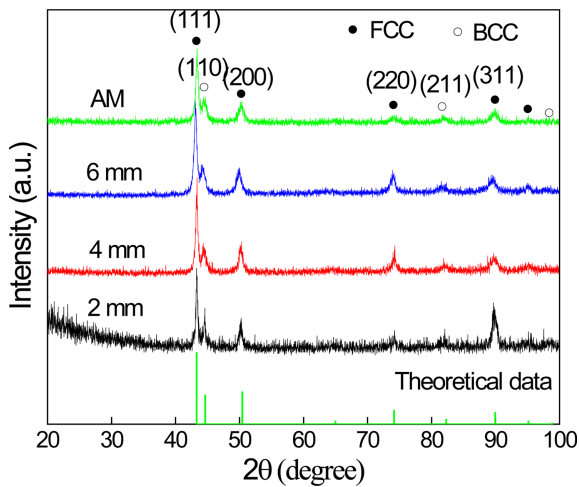
Fig. 2. (Color online) XRD patterns of FeCoNi(CuAl)$_{0.8}$ HEAs with different cooling rates.

structure [4, 16, 17]. Therefore, the increased value of M_s with the increase of cooling rate may be attributed to the increase in the volume fraction of the BCC phase in the alloy. Furthermore, the lattice parameters of both FCC and BCC decrease with the increasing of cooling rate, indicating that a higher cooling rate results in a higher stacking density, which may also contribute to the increase of saturation magnetization due to more ferromagnetic

atoms being involved. In addition, (311) peak of the 2 mm sample is extremely high compared with the theoretical diffraction pattern of randomly oriented samples, indicating that the 2 mm sample is strongly textured. This texture phenomenon is also found in the Fe$_{63}$Co$_{32}$Gd$_5$ alloy ribbons prepared at a high cooling rate [18]. This phenomenon will certainly affect its magnetic properties. But the mechanism is not clear at present and should be further studied.

It was reported that the saturation magnetization is mainly determined by the composition and atomic-level structures, but H_c is sensitive to the grain size [11, 19]. In order to understand the mechanism of how H_c is affected by cooling rate, the microstructure of the alloys should also be studied. Fig. 3 is phase morphologies of the alloys prepared at different cooling rates. a1, b1, c1 and d1 in Fig. 3 are SEM images of the dendritic phases at the relative edge of the AM, 6 mm, 4 mm and 2 mm samples, a2, b2, c2 and d2 are equiaxed grains at the center of the samples, and a3, b3, c3 and d3 are high-resolution images of the corresponding dendritic phases (marked by wireframe or white arrows). It's obviously that the grain size decreases with increase of the cooling rate, especially the grain size of the 2 mm sample is much smaller than the samples prepared at low cooling rates. For instance, the primary and secondary dendritic arm spacing of the AM
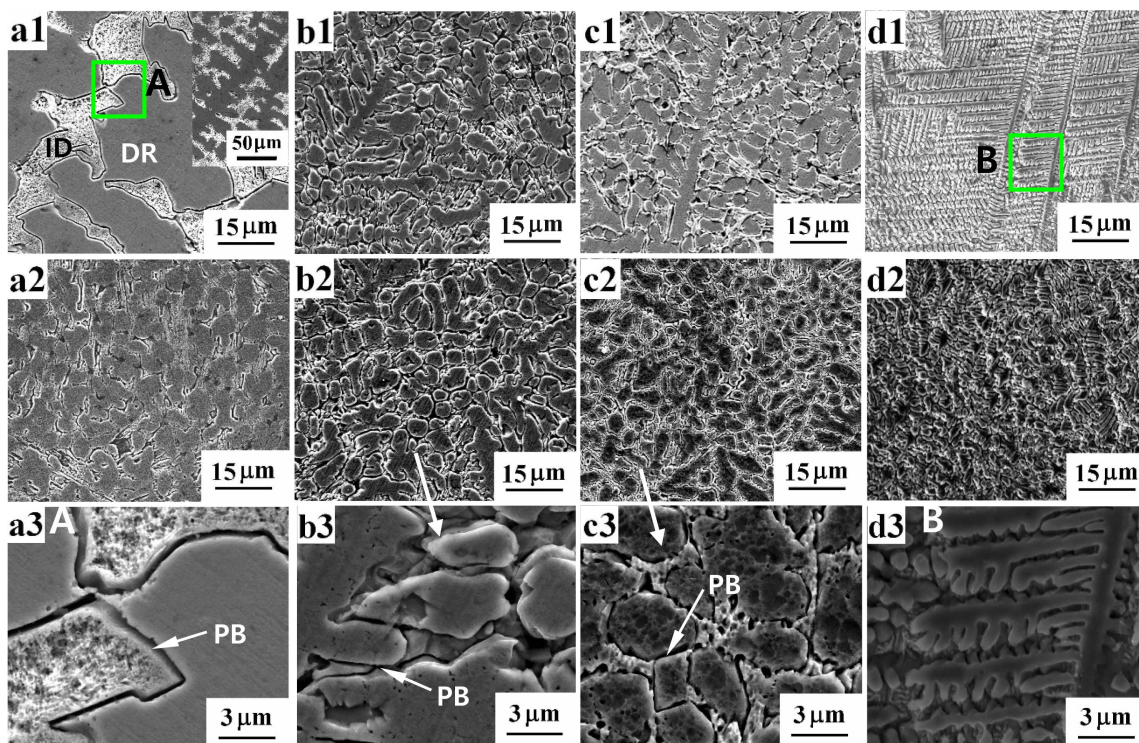

Fig. 3. (Color online) SEM images of the alloys at different magnitudes: (a1)-(a3) AM alloys; (b1) and (b3) 6 mm; (c1) and (c3) 4 mm; (d1) and (d3) 2 mm.

sample decreases from approximately 70 μm and 20 μm to 12 μm and 3 μm of the 2 mm sample, respectively. Generally, a large undercooling degree induced by a high cooling rate can stimulate more nucleation sites and produce finer grains. Finer grains usually mean more grain boundaries, which can act as pinning sites to hinder the magnetic domain wall movement, thus causing high coercivity [16]. Therefore, H_c increases with the increasing of cooling rate. Furthermore, it is interesting that the AM sample and 6 mm sample, which are cooled at different rates, nearly have the same M_s and H_c, which may be because the central regions of the two samples chosen for VSM tests have the similar microstructures.

Furthermore, all the samples exhibit typical cast dendritic (labeled as DR) phases and interdendritic (labeled as ID) phases. According to the XRD results, the relative volume fraction of the FCC phase is much larger than the BCC phase, so it is possible that the DR regions are FCC phases, and the ID regions are BCC phases. The results are consistent with Zhang's study [4]. In addition, there are phase boundary (labeled as PB) regions between the DR and ID regions, which can be seen from the high-resolution images in Fig. 2(a3) and Fig. 2(b3). And the thickness of the PB regions for different samples has a great difference, which may be related to elemental segregation in the solidification process. These phenomena are similar to those of conventional alloys.

Element distributions across different regions of the AM sample are shown in the line-scans in Fig. 4. Fig. 4(a) shows backscattered electron image and the corresponding line-scans. It can be seen that the contents of Al and Ni in the ID region and PB region are much higher than the contents in DR region, while the contents of Fe and Co in the DR region are much higher than the contents in the ID region. Cu content is almost the same in the DR region and the ID region, but it is seriously enriched in the PB region. Interestingly, the Ni and Cu distribution results are quite different from Zhong's study [5]. Fig. 4(b) shows line-scans of the sample with PB region corroded. The differences of element content in the three regions are more obvious. The steep drop in the contents of Cu and Al at grain boundaries confirmed on the other side that Cu and Al are enriched in the PB region. The element distribution may be understood by the mixing enthalpy and melting points difference of the elements. The melting points and mixing enthalpies of different elements are shown in Table 2 [5]. First, dendritic phases enriched with Fe and Co are formed due to the high melting points of Fe and Co elements during the solidification process. At the same time, a small amount of Ni and Cu are expelled due to the nonnegative mixing enthalpies of Co-Ni, Fe-Cu and Cu-Co, and Al is
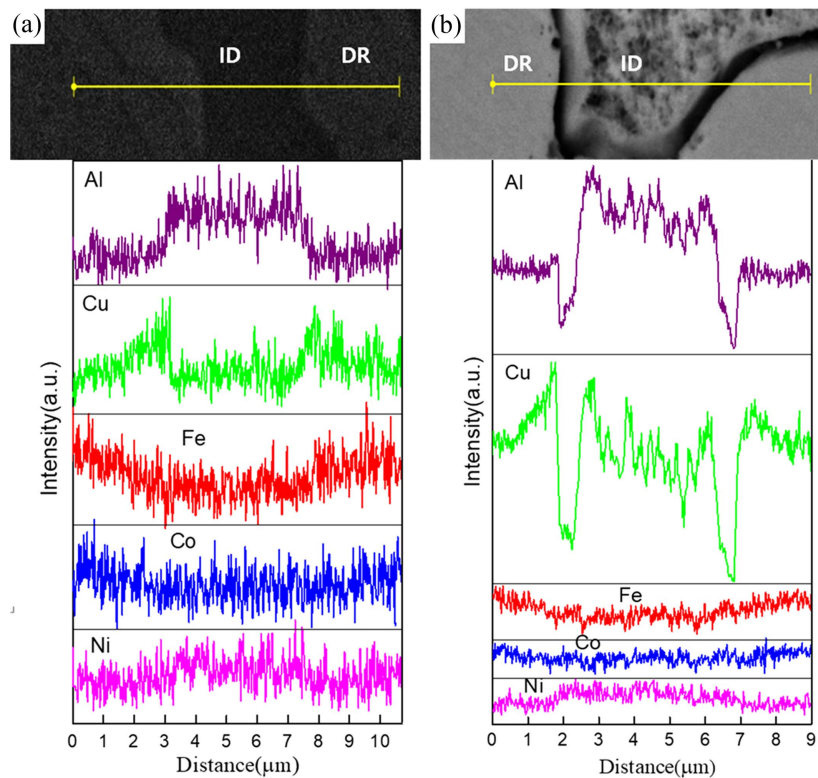

Fig. 4. (Color online) Elemental distribution across the grains of the AM sample: (a) polished sample, (b) corroded sample.

Table 2. The melting points of different elements (K) and the mixing enthalpies between two elements (kJ/mol) [5].

Element	T_m/K	Fe	Co	Ni	Cu
Fe	1808	-	-	-	-
Co	1767	-1	-	-	-
Ni	1726	-2	0	-	-
Cu	1358	13	6	4	-
Al	933	-11	-19	-22	-1

expelled due to the lower melting points. Then the rest of elements solidify and form the interdendritic phases, and in this process, Cu is also expelled by the interdendritic phases due to the positive mixing enthalpy of Co-Cu and Ni-Cu. Therefore, the DR region and ID region form FeCo-rich phase and NiAl-rich phases, respectively, while Cu is expelled to the PB region by both DR and ID regions due to the positive mixing enthalpies of Cu-Co, Fe-Cu and Cu-Ni.

TEM images of AM sample and the sample with diameter of 4 mm are compared in Fig. 5. DR, PB, and ID regions of the samples can be observed in Fig. 5(a1) and (b1). The DR region is verified to be an FCC structure by the corresponding selected-area-electron-diffraction (SAED), as shown in Fig. 5(a3), which is consistent with

the XRD result. And the additional superlattice electron diffraction spots in Fig. 5(a3) indicate that the DR region is an ordered FCC structure. Some ring dislocations are visible in the DR region of the 4 mm sample (marked with arrows in Fig. 5(a1)), but are not in the DR region of the AM sample, indicating that an higher cooling rate exerts more defects to the alloy due to severe lattice distortion. It is a general characteristic for all the solidified alloys that the residual stress and lattice distortion increase with the increase of cooling rate. All the defects, severe lattice distortion, and residual stress will increase the difficulty of domain wall movement, leading to the increase of coercive force. Similar phenomenon can also be found in Gao's study [20].

Furthermore, it can be seen that the width of the PB region in the AM sample, which has been corroded, is much wider than that in the 4 mm sample, which is consistent with the SEM result in Fig. 3. The enlarged images of the ID region for the two samples are compared in Fig. 5(a2) and (b2). It can be clearly seen that there are numerous nanoprecipitates embedded in the ID region of both the two samples. These were verified to be FCC nanoprecipitates embedded in the BCC matrix by the corresponding SAED, as shown in Fig. 5(b3). Nevertheless, more and finer nanoprecipitates embedded in the sample
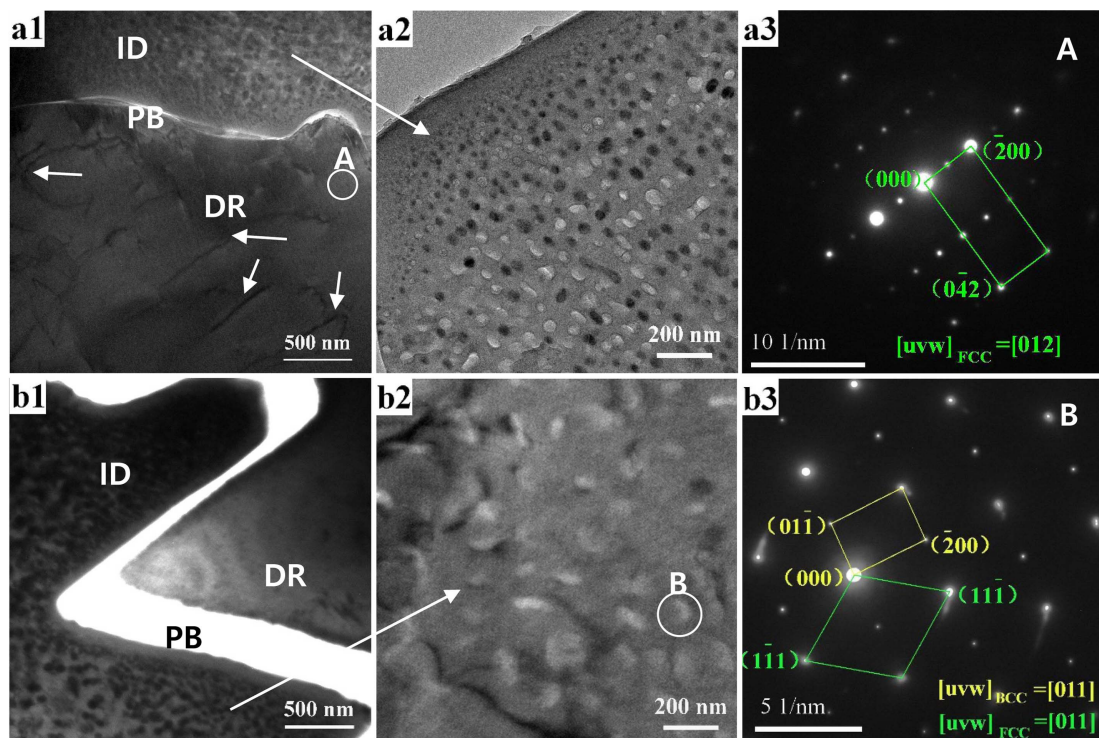

Fig. 5. (Color online) TEM images of AM sample and the sample with diameter of 4 mm: (a) and (d) bright-field images of the AM sample and the sample with diameter of 4 mm, respectively; (b) and (e) bright-field images of the ID region in the AM sample and the sample with diameter of 4 mm, respectively; (c) and (f) the corresponding SAED images of region A and B in the AM sample, respectively.

prepared at relatively higher cooling rate. For example, the average size of the nanoprecipitates reduced from 50-80 nm in the AM sample to 20-50 nm in the 4 mm sample. Element distributions show that these nanoprecipitates are enriched in Cu element. Cu is diamagnetic, so these nanoprecipitates themselves may not significantly affect the magnetic properties of these alloys. However, more nanoprecipitates may provide more pinning points, preventing the domain wall movement and increasing the coercive force.

In addition, the nanoprecipitates become finer near the grain boundary, and within an 80 nm scope of the grain boundary there is a precipitate-free zone for the 4 mm sample. But for the AM sample, the width of the precipitate-free zone enlarges to 100 nm. Normally, the larger the sample size, the slower the solidification. Therefore, there is more time to exclude Cu elements to the grain boundary in the solidification process, leading to a wider precipitate-free zone.

4. Conclusions

In order to understand the mechanism and effect of cooling rate on the magnetic properties of FeCoNi(CuAl)$_{0.8}$ HEAs, hysteresis loops and microstructures of the HEAs with different sizes were systematically investigated. The main conclusions are summarized as follows:

(1) All the samples prepared with different cooling rates have a duplex-phase structure of face-centered cubic (FCC) plus body-centered cubic (BCC).

(2) All the samples are good soft magnetic alloys with high M_s and low H_c, and M_s and H_c of the samples gradually increase with the increasing of cooling rate.

(3) Microstructure investigation shows that the stacking density and volume fraction of BCC phase in the alloy increase with the increase of cooling rate, leading to an increased value of M_s. while the increased value of H_c for the sample prepared at a relatively higher cooling rate may be attribute to the decreased grain size, severe lattice distortion, residual stress, and more nanoprecipitates embedded in the ID region.

Acknowledgment

Conflict of Interest

There are no conflicts of interest.

References

[1] R. Motallebi, Z. Savaedi, and H. Mirzadeh, Arch. Civ. Mech. Eng. **22**, 1 (2022).

[2] L. J. Lin, X. Xian, Z. H. Zhong, K. J. Song, C. Y. Wang, G. Q. Wang, Y. C. Wu, and P. K. Liaw, Adv. Compos. Hybrid Mater. **5**, 1508 (2022).

[3] X. F. Gao, R. R. Chen, T. Liu, H. Fang, G. Qin, Y. Q. Su, and J. J. Guo, J. Mater. Sci. **57**, 6573 (2022).

[4] Q. Zhang, H. Xu, X. H. Tan, X. L. Hou, S. W. Wu, G. S. Tan, and L.Y. Yu, J. Alloys Compd. **693**, 1061 (2017).

[5] Z. Li, H. Xu, Y. Gu, M. X. Pan, L. Y. Yu, X. H. Tan, and X. L. Hou, J. Alloys Compd. **746**, 285 (2018).

[6] V. E. Gromov, Yu. A. Shlyarova, S. V. Konovalov, S. V. Vorob'ev, and O. A. Peregudov, Steel in Translation **51**, 700 (2021).

[7] K. A. Osintsev, V. E. Gromov, S. V. Konovalov, Yu. F. Ivanov, and I. A. Panchenko, Steel in Translation **52**, 167 (2022).

[8] X. Z. Lim, Nature **533**, 306 (2016).

[9] J. F. Wang, R. Li, N. B. Hua, and T. Zhang, J. Mater. Res. **26**, 2072 (2011).

[10] Q. Zhang, Z. Z. Li, G. Q. Zhang, W. Zheng, X. Cao, X. D. Hui, and S. X. Zhou, J. Mater. Sci.-Mater. El. **33**, 10259 (2022).

[11] R. Wei, H. Sun, C. Chen, Z. Han, and F. S. Li, J. Magn. Magn. Mate. **435**, 184 (2017).

[12] R. Wei, J. Tao, H. Sun, C. Chen, G. W. Sun, and F. S. Li, Mater. Lett. **197**, 87 (2017).

[13] F. J. Wang, Y. Zhang, G. L. Chen, and H. A. Davies, Journal of Engineering Materials and Technology **131**, 034501 (2009).

[14] L. L. Ma, C. Li, Y. L. Jiang, J. L. Zhou, L. Wang, F. C. Wang, T. Q. Cao, and Y. F. Xue, J. Alloys Compd. **694**, 61 (2017).

[15] X. H. Lin and W. L. Johnson, J. Appl. Phys. **78**, 6514 (1995).

[16] M. Zhu, C. Zhang, K. Li, Y. Q. Liu, M. Zhang, L. J. Yao, and Z. Y. Jian, Acta Metall. Sin. **34**, 1557 (2021).

[17] Y. F. Kao, S. K. Chen, T. J. Chen, P. C. Chu, J. W. Yeh, and S. J. Lin, J. Alloys Compd. **509**, 1607 (2011).

[18] W. J. Yao, N. Wang, and J. H. Lee, J. Cent. South Univ. **22**, 2014 (2015).

[19] P. P. Li, A. Wang, and C. T. Liu, J. Alloys Compd. **694**, 55 (2017).

[20] J. E. Gao, H. X. Li, F. Jiang, B. Winiarski, P. J. Withers, P. K. Liaw, and Z. P. Lu, Metallurgical and Materials Transactions A-Physical Metallurgy and Materials Science **44A**, 2004 (2013).